Journal of Molecular Modeling (2023) 29:195
https://doi.org/10.1007/s00894-023-05599-0

ORIGINAL PAPER

Progress in theoretical study of lead-free halide double perovskite Na_2AgSbX_6 (X = F, Cl, Br, and I) thermoelectric materials

Sunita Kumari[1] · Peeyush Kumar Kamlesh[2] · Lalit Kumari[3] · Sudhir Kumar[3] · Sarita Kumari[1] · Rashmi Singh[4] · Rajeev Gupta[5] · Manendra S. Chauhan[6] · Upasana Rani[7] · Ajay Singh Verma[7,8]

Received: 25 February 2023 / Accepted: 20 May 2023 / Published online: 1 June 2023

Abstract

Context Herein, we have studied progressively novel metal lead-free halide double perovskite renewable energy materials. Due to their potential use in electronic devices, researchers have investigated these materials with a lot of interest. From the electronic structure, we have found that these are the indirect band gap semiconductors within the range between 1.273 and 3.986 eV. Optical parameters such as dielectric constant, electrical conductivity, and absorption coefficient have also been investigated, which have shown that these materials have potential use in photovoltaics. We have checked stability issues by thermodynamic parameters and phonon spectra. We have found them thermally stable; however, the phonon spectra show their dynamical instability and except for Na_2AgSbF_6 and Na_2AgSbI_6, the remaining compounds are weak in mechanical stability. For another futuristic purpose, thermoelectric parameters such as Seebeck coefficient, power factor, and figure of merit have also been calculated, which again verifies that these materials may be very useful in thermoelectric devices. Most of the parameters have been computed for the first time.

Methods We have performed this computational work using WIEN2k simulation code, which is based on the full-potential linearized augmented plane wave (FP-LAPW) technique. It is one of the most reliable techniques to calculate the photovoltaic properties of semiconducting perovskites. The interaction between ion-core and valence electrons was dealt with within the PAW technique as implemented in Vienna Ab initio Simulation Package (VASP).

Keywords Halide double perovskite · Dielectric constant · Refractive index · Seebeck coefficient · Figure of merit

Introduction

The growing global need for energy has created an alarming situation, which can be sorted out with the help of renewable energy resources. Photovoltaic is the best option in the field of renewable energies. The Sun is a conventional resource of sustainable and long-term supply of energy. Solar cells, which are based on the photovoltaic effect, are useful to convert solar energy into electricity. The great interest of the industry is to develop new solar cell devices with high efficiency, good intrinsic stability, and lower production costs. Perovskite is a substance with the chemical formula ABX_3, where X is an anion and A and B are cations [1]. A rapid increase in the record power conversion efficacies of

✉ Ajay Singh Verma
ajay_phy@rediffmail.com

[1] Department of Physics, University of Rajasthan, Jaipur, Rajasthan 302004, India

[2] School of Basic and Applied Sciences, Nirwan University Jaipur, Jaipur, Rajasthan 303305, India

[3] Department of Applied Physics, Mahatma Jyotiba Phule Rohilkhand University, Bareilly, Uttar Pradesh 243006, India

[4] Department of Physics, Institute of Applied Sciences & Humanities, G. L. A. University, Mathura, Uttar Pradesh 281406, India

[5] Department of Physics, School of Engineering, University of Petroleum & Energy Studies, Dehradun, Uttarakhand 248007, India

[6] School of Allied Sciences, Dev Bhoomi Uttarakhand University, Dehradun, Uttarakhand 248007, India

[7] Division of Research & Innovation, School of Applied and Life Sciences, Uttaranchal University, Dehradun, Uttarakhand 284007, India

[8] University Centre for Research & Development, Department of Physics, Chandigarh University, Mohali, Punjab 140413, India

photovoltaics is found from 3.8% in 2009 to more than 25% nowadays [2]. Various anti- and hybrid perovskite materials have been investigated for renewable energy applications [3–6]. We have also calculated the efficiency of the oxide-based perovskites for photovoltaic applications, and it is found that the PCE of these perovskites has grown more than 20% [7]. An organic–inorganic lead halide perovskite shows preferable photovoltaic properties like low effective electron and hole masses, enormously high optical absorption coefficients, large carriers' diffusion lengths and lifetimes, and tunable band gap [8] while having two issues: One is the Toxicity of Pb^{+2} ions, and the second is instability in air and heat due to the organic part of $MAPbI_3$.

@@Toxic divalent Pb^{+2} is replaced by monovalent and trivalent cations, and the perovskite structure looks like $A_2^{+1}M^{+1}M^{-+3}X_6^{-1}$. The structure with the general formula $A_2^{+1}M^{+1}M^{-+3}X_6^{-1}$ is known as the double perovskite structure and has been proposed for use to overcome these issues. Lead-free double perovskites are found to be more stable under sufficient humidity and temperature and show better solar efficiencies with non-toxicity [9–11]. These double perovskites have photovoltaic properties like low charge carriers' effective mass, long charge carriers' lifetime at room temperature, and larger stability in air and heat than lead halide perovskites [12]. Some more advantages of lead-free double perovskites include minimal defects, great optical absorption, an appropriate band gap, and extremely high stability [13–19].

The one drawback of earlier investigated double perovskites is that they mostly have too large band gap for use in solar cell devices. Hence, there is a high need to design a double perovskite with a tunable band gap within the solar spectrum. So, currently, the objective of the scientific community is not only focused on the stability and enhancing the power conversion efficiency of solar cells and thermoelectric devices but also to find easy processes and lower production cost technologies. The double perovskite with mixed halides is also a way to develop perovskites with tunable band gaps [20]. Muscarella et al. [21] have explained the applications of these types of materials in numerous areas. They mentioned that other than photovoltaics, these materials can also be utilized as X-ray detectors, light-emitting diodes, memory devices, indoor photovoltaics, temperature and humidity sensors, photocatalysts, etc. A vast study has been done on cesium-based halide double perovskites [10–24] which reveals the potential of lead-free inorganic halide double perovskites in photovoltaic, thermoelectric, and other indoor and outdoor devices. Al-Qaisi et al. [25] have investigated Na_2CuMCl_6 (M = Bi, Sb) double perovskite and found that these are small band gap semiconductor materials and exhibit high potential for optoelectronic devices having high absorption, high optical conductivity, and low reflectivity. They have also studied transport properties with chemical potential (μ) and found that their figure of merit (ZT) approaches unity, which shows their potential in thermoelectric devices also. Asghar et al. [26] have also explained the potential of Rb_2ScAgX_6 (X = Cl, Br, I) halide-based double perovskite in optoelectronic and thermoelectric devices. Dar et al. [27] have done a computational study of half-metallic halide double perovskites: Cs_2KXCl_6 (X = Co and Ni). They investigated the structural stability of these materials as well as the origins of half-metallicity and predicted them as potential candidates in spintronic devices. Nawaz et al. [28] have reported DFT calculation results for investigating the structural stability of Rb_2YInX_6 (X = Cl, Br, I) double perovskites including their optoelectronic and transport parameters. They concluded that they are semiconductors with direct and significant band gaps and may be taken into account for optoelectronic and thermoelectric devices. Cs_2NaBiI_6 lead-free double perovskite material has been recommended by Zheng et al. [29] for its good memory behavior even after 90 days of air exposure or with a rise in temperature up to 403 K. From the above-cited literature, we note that because of their exceptional performance, non-toxicity, and environmental sustainability, halide double perovskite materials are subsequently being recommended as high-performing semiconductors, primarily for solar and thermoelectric devices [30]. In this context, we have looked at the structural, electrical, optical, and thermoelectric characteristics of novel lead-free inorganic halide-based double perovskites Na_2AgSbX_6 (X = F, Cl, Br, and I). These are made up of non-toxic and easily available elements in nature.

Methodology

We have performed this computational work using the WIEN2k simulation code [31], which is based on the full-potential linearized augmented plane wave (FP-LAPW) technique. It is one of the most reliable techniques to calculate the photovoltaic properties of semiconducting perovskites. The unit cell was divided using this technique into non-overlapping atomic spheres that are situated around the atomic sites and an interstitial site. The potential was taken to be constant outside the atomic spheres but spherically symmetric inside them for the purpose of building basis functions (muffin-tin approximation, MTA). Atomic-like wave functions were used for the atomic sphere region, and plane waves were employed at the interstitial site. This method was used within density functional theory (DFT). DFT has the highest degree of accuracy, and the ability to handle periodic as well as non-periodic systems with many electrons, hence, becomes a popular method for calculation. DFT works on the basic principle which is used to describe an interacting system of fermions by using its density of electrons instead of the many-body wave function. The main issue with DFT is that it only recognizes the free electron gas

as the precise functional for exchange and correlation. However, approximations survive which allows the computation of definite physical quantities fairly exactly. Hence, there is a necessity to use approximations. In this study, we used the generalized gradient approximation configured by Perdew-Burke-Ernzerhof (PBE-GGA) [32]. The atomic positions and lattice constant have been fully optimized until the energy and charge converged to 10^{-4} Ry and 10^{-3} *e* correspondingly. The cutoff energy, or the energy separating the core and valance states, was set to − 10 Ry. The shortest muffin tin radius, R_{MT}, and the plane wave cutoff vector, K_{max}, together yield a convergent solution with $R_{MT}K_{max} = 7$. The charge density's Fourier expansion's greatest vector, G_{max}, is described by its magnitude and was assumed to be 12. A mesh of 1000 k-points in the Brillouin zone was used for structural optimization of the compounds. A denser mesh with 10,000 k-points was used to calculate the compounds' electrical, optical, and thermoelectric properties. Using the BoltzTraP algorithm, all thermoelectric parameters were computed in terms of chemical potential [33]. In solid-state research and materials developments, the determination of thermodynamical parameters is crucial to better comprehend the fundamental properties of composites under high temperature and pressure conditions. This investigation used the quasi-harmonic Gibbs2 code [34] to calculate the material's thermal stability. The mechanical stability of the titled materials has been checked by computing the elastic properties using the IRElast package incorporated in WIEN2k. Plane wave–based DFT calculations combined with phonons lattice dynamics were carried out to examine the dynamical stability of the Na_2AgSbX_6 (X = F, Cl, Br, I) perovskite system. The interaction between ion-core and valence electrons was dealt with within the PAW [35, 36] technique as implemented in Vienna Ab initio Simulation Package (VASP) [37]. The valence electron configurations of the elements present in the subject line composition are Na ($3s^1$), Ag ($4d^{10}$, $5s^1$), Sb ($5s^2$,$5p^3$), F ($2s^2$,$2p^5$), Cl ($3s^2$,$3p^5$), Br ($4s^2$,$4p^5$), and I ($5s^2$,$5p^5$). A Monkhorst–Pack technique with an 8 × 8 × 8 k-point mesh and a plane wave basis set's kinetic energy cutoff of 520 eV was employed for the Brillouin zone sampling. During the geometric optimization, the forces were minimized up to 10^{-3} eV/Å. The dynamical properties were calculated within harmonic approximations using the PHONOPY program [38]. To compute the phonons, we have considered 2 × 2 × 2 cell (80 atoms) of the subject line composition on top of their primitive cell using the finite displacement method [39].

Results and discussions

Structural properties

Na_2AgSbX_6 (X = F, Cl, Br, and I) halide double perovskite materials crystallize in the $Fm\bar{3}m$ (#225) space group. The structure of their conventional cell with Wigner–Seitz cell and primitive cell is represented in Fig. 1. We reduce the energy of these compounds as a function of volume in order to get the ideal ground state, and further, these changes in energy versus volume are fitted to the Birch-Murnaghan equation of state [40]. The energy versus volume curve of the studied materials is presented in Fig. 2. From this energy-volume fitting curve, we have determined various structural parameters such as the lattice constant (*a* in Å), bulk modulus at zero pressure (B_0 in GPa), its first pressure derivative (B_0'), and the total ground state energy (E_0 in Ry) and presented in Table 1. From this, it is understood that the lattice constant of these materials increases with the increasing size of the halogen atom. The computed lattice parameters are in best agreement with that of some other materials listed in Table 1. A further structural factor that describes a compound's resilience under pressure is its bulk modulus. We see that it follows just the opposite behavior of the lattice constant, which describes that the heavier material is more compressible. The pressure derivative of bulk modulus for all these materials has been observed as positive. It demonstrates that these compounds can stiffen under increased pressure. The − ve values of total ground state energy of these materials exhibit that all of these materials are stable and the stability of these materials increases for heavier materials. The variation of the lattice parameters with the size of the X-atom confirms our study's accuracy and reliability.

Electronic properties

To perform the SCF simulations, the optimized structural factors were considered with PBE-GGA exchange–correlation potential functional. As we know that the PBE-GGA underestimates the band gap, so to enhance its value near

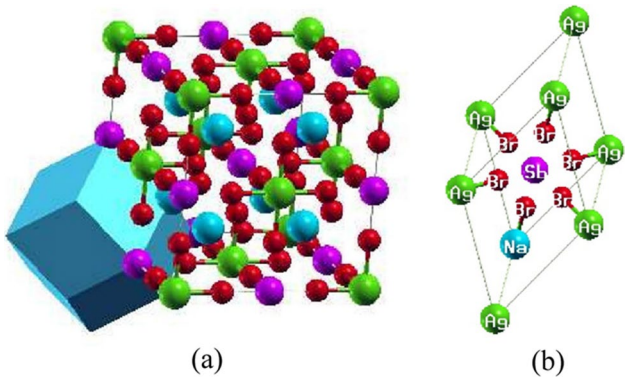

Fig. 1 **a** Conventional cell with Wigner–Seitz cell and **b** primitive cell of Na_2AgSbX_6 (X = F, Cl, Br, and I), where blue atom represents Na-atom, green atom represents Ag-atom, purple atom represents Sb-atom, and red atom represents X-atom

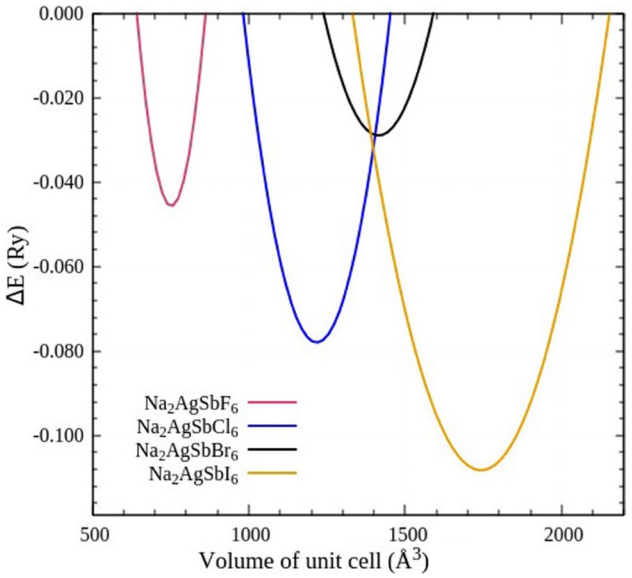

Fig. 2 Volume optimization curve of Na_2AgSbX_6 (X = F, Cl, Br, and I)

to its experimental value, we can use Becke-Johnson Potential modified by Koller, Tran, and Blaha (KTB-mBJ) as implemented by Soni et al. [41] to investigate halide double perovskite materials. The band structure curves for these materials' first Brillouin zone, plotted between wave vector "k" and their energy function, are shown in Fig. 3a–d. These band structure plots exhibit that the studied materials have an indirect band gap (X-L). Table 1 includes information about these compounds' band gap. The band gap trend in this table can be interpreted as follows: The band gap of these compounds declines as the atomic number of the X-atom increases, supporting the theoretical idea of the trend of variations in the energy band gap. A comparison of band gap of the titled materials with some other relatable materials using PBE and PBE + KTB-mBJ has been shown in Table 1, which further confirms the reliability of the computed results for the studied materials.

We have calculated the total and partial densities of states (DoS) of these compounds, and their plots have been showcased in Fig. 4, which will enable us to better comprehend how the interaction between the atoms' various orbitals works. For each compound, in the lower valence band section (< − 2 eV), the major peaks are produced by the *p*-orbital of Sb and X-atom (X = F, Cl, Br, and I) with a tiny contribution from the *d*-orbital of Ag-atom. Peaks arise in the upper valence band section (between − 2 and 0 eV) due to the substantial contribution of the *d*-orbital of Ag-atom and the modest contribution of the *p*-orbital of X-atom and *s*-orbital of Sb, while sodium atom's contribution is negligible. In the conduction band, the resultant peak of total DoS appears due to the *p*-orbital of Sb and X-atom, whereas other atoms show negligible contribution. Thus, the study of DoS reveals the contribution of various atoms near the Fermi level.

Optical properties

Optical parameters including dielectric constant $\varepsilon(\omega)$, optical conductivity $\sigma(\omega)$, and refractive index n(ω) have been calculated using optimized structural and electronic parameters in WIEN2k code for the incident electromagnetic energy range (0–13 eV), as shown in Figs. 5 and 6. These optical properties highlight a material's significance in optoelectronic applications by describing how it responds to electromagnetic (EM) radiation. The dielectric function defines a material's linear response to incident electromagnetic radiation by explaining how photons interact with a material's electrons. It is a complex quantity and can be defined by Ehrenreich and Cohen's equation [42] as mentioned below:

$$\varepsilon(\omega) = \varepsilon_1(\omega) + i\varepsilon_2(\omega) \quad (1)$$

Electronic polarization and anomalous dispersion are associated with its real part $\varepsilon_1(\omega)$, while optical absorption can be defined by its imaginary component $\varepsilon_2(\omega)$.

The Kramers–Kronig transformation equation [43] can be used to compute the real component of the dielectric tensor $\varepsilon_1(\omega)$ by using its imaginary component $\varepsilon_2(\omega)$. Other residual optical properties such as optical conductivity $\sigma(\omega)$, extinction coefficient k(ω), reflectivity R(ω), absorption coefficient $\alpha(\omega)$, refractive index n(ω), and energy loss function $E_{loss}(\omega)$ can be calculated with the help of $\varepsilon_1(\omega)$ and $\varepsilon_2(\omega)$ [44].

Table 1 Structural, electronic, and optical parameters of Na_2AgSbX_6 (X = F, Cl, Br, and I)

Compound	a (Å)	B_0 (GPa)	B_0'	E_0 (Ry)	Bandgap (eV)		Dielectric constant $\varepsilon_1(0)$	Refractive index n(0)	Reflectivity R(0)
					PBE	PBE + KTB-mBJ			
Na_2AgSbF_6	9.056	52.693	4.776	− 25,450.646	1.322	3.986	3.713	1.974	0.549
$Na_2AgSbCl_6$	10.648, 10.83[a]	29.856	4.855	− 29,790.378	1.273, 1.239[a]	2.833, 2.212[a]	5.327	2.346	0.479
$Na_2AgSbBr_6$	11.192, 11.38[a]	25.066	4.642	− 55,531.93	0.784, 0.762[a]	2.108, 1.571[a]	6.745	2.637	0.592
Na_2AgSbI_6	11.988, 12.16[a]	19.841	5.221	− 109,680.708	0.330, 0.312[a]	1.273, 0.876[a]	9.005	3.040	0.641

[a]Reference [41] for Cs_2AgSbX_6 (X = Cl, Br, I)

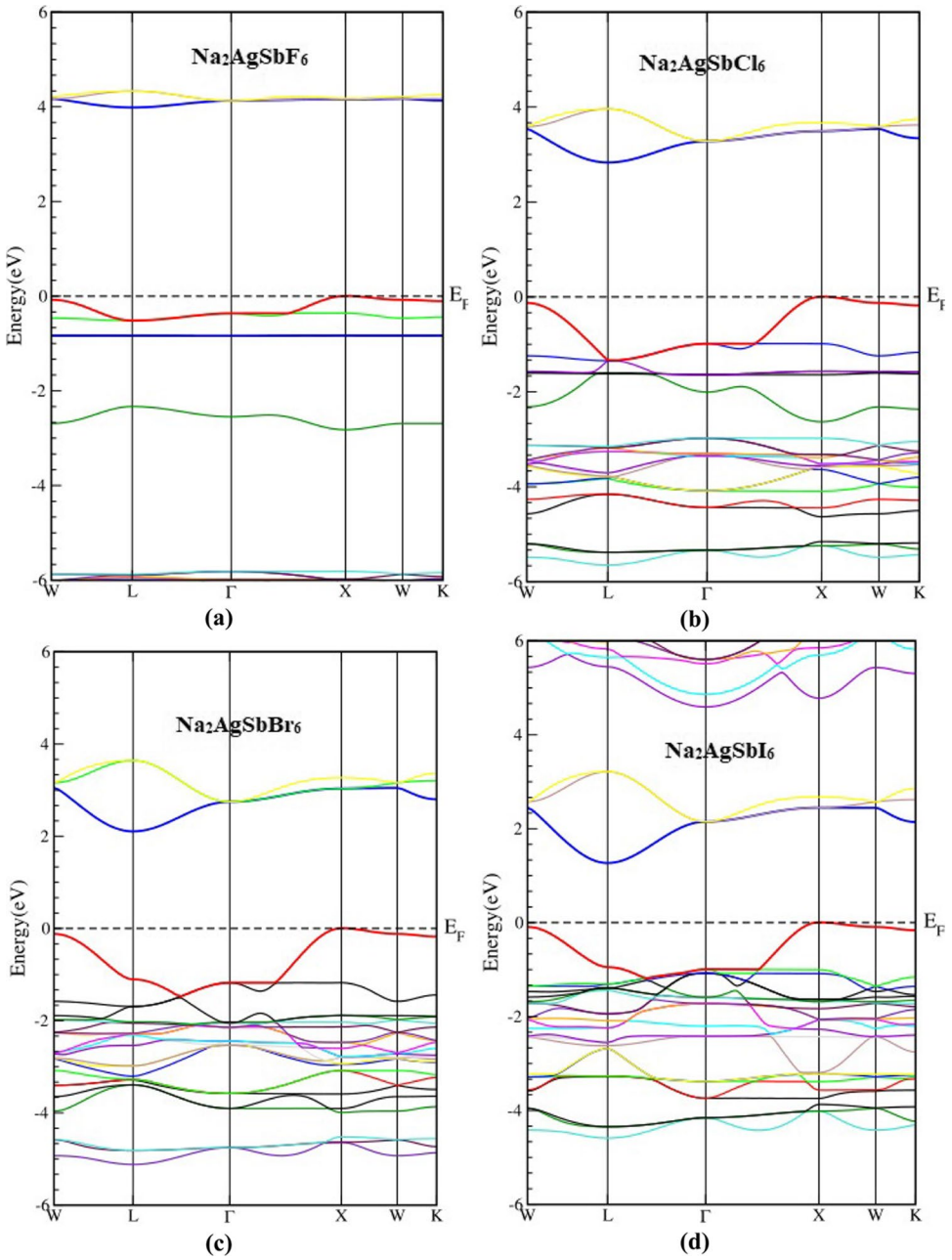

Fig. 3 Band structure of Na_2AgSbX_6 (X = F, Cl, Br, and I)

The calculation of these characteristics demonstrates that these materials are homogenous and isotropic, i.e., values of their various optical parameters change with frequency but remain constant with respect to the direction of incident EM radiation's electric field vector. Figure 5(a) and (b) represent the real and imaginary component of the dielectric tensor spectra $\varepsilon(\omega)$ correspondingly for the varying energies of incident radiation. The dielectric constant of a substance is expressed by the static value of its real component $\varepsilon_1(0)$, which can be characterised by a small perimeter of energy. The value of $\varepsilon_1(0)$ for Na_2AgSbX_6 (X = F, Cl, Br, and I) is calculated as 3.713, 5.327, 6.745, and 9.005, respectively. A material's stronger reactivity to the incident energy is caused by the larger value of $\varepsilon_1(0)$. For the titled materials, the fluctuation in $\varepsilon_1(\omega)$ with respect to the incident energy is depicted in Fig. 5(a). This figure clearly shows that for these materials, the value of $\varepsilon_1(\omega)$ rises quickly with the incident energy, reaches its highest value, then decreases with some peaks and valleys, and turns negative above 7 eV. Finally, a modest increase approaching zero is recorded. While the peak of $\varepsilon_1(\omega)$ is noticed in the near-infrared area for Na_2AgSbI_6, it is observed in the visible range for all other materials, meaning that these compounds respond most strongly in the relevant regions. According to Fig. 5(b), the threshold energy of $\varepsilon_2(\omega)$ for these materials falls between 1.286 and 4.120 eV. The threshold energy value illustrates a

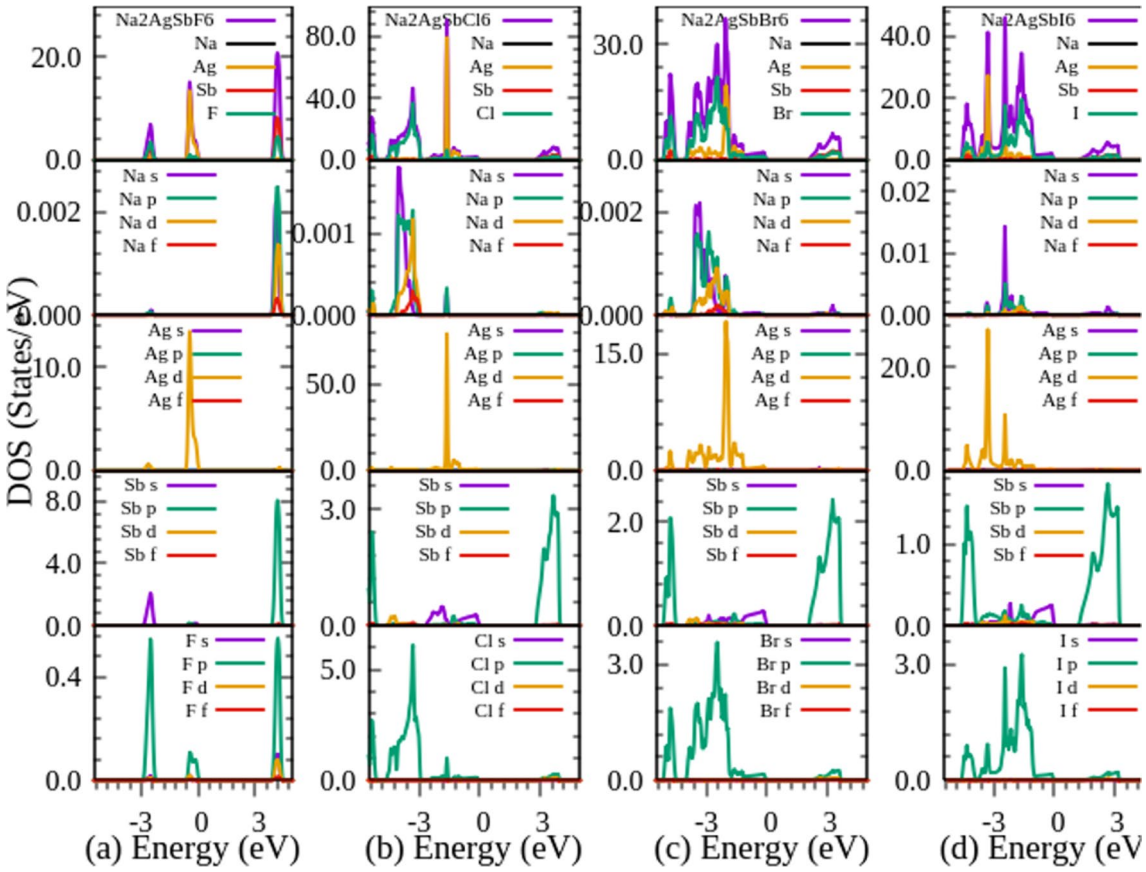

Fig. 4 Total and partial DOS plots for Na_2AgSbX_6 (X = F, Cl, Br, and I)

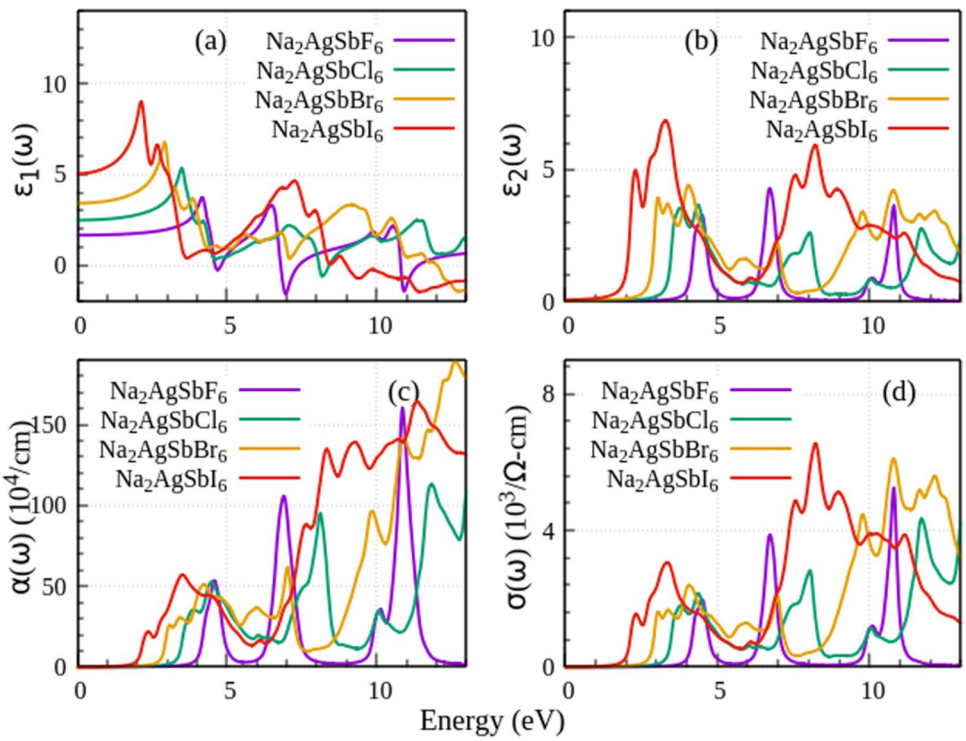

Fig. 5 (**a**) Re part of dielectric constant $\varepsilon_1(\omega)$, (**b**) Im part of dielectric constant $\varepsilon_2(\omega)$, (**c**) absorption coefficient $\alpha(\omega)$, and (**d**) optical conductivity $\sigma(\omega)$ for Na_2AgSbX_6 (X = F, Cl, Br, and I)

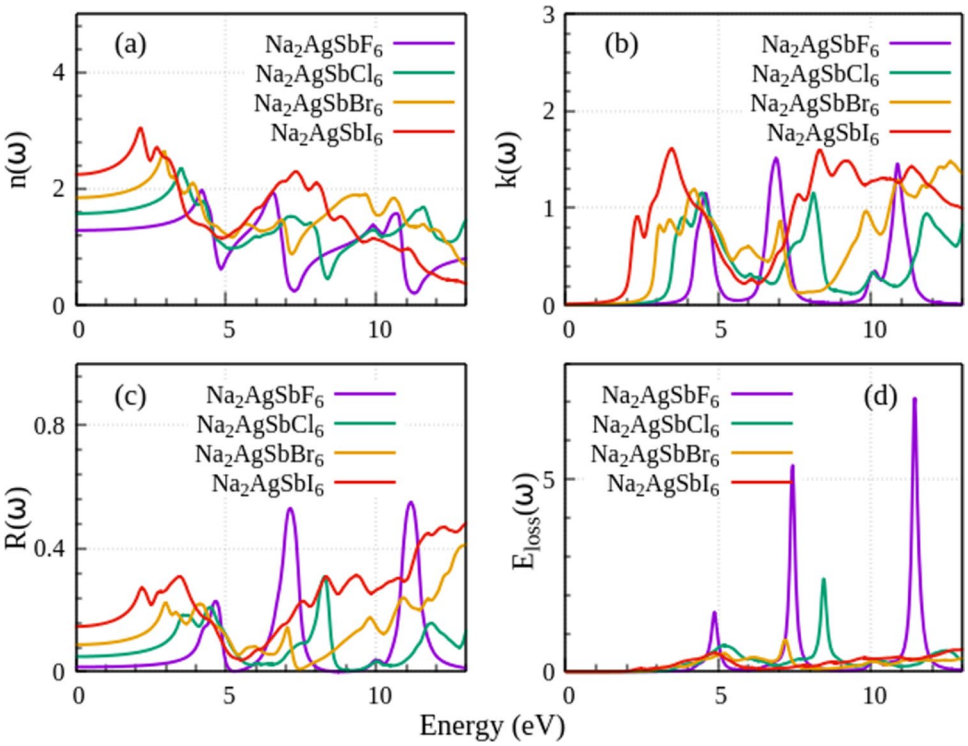

Fig. 6 (**a**) Refractive index n(ω), (**b**) extinction coefficient k(ω), (**c**) reflectivity R(ω), and (**d**) energy loss function $E_{loss}(\omega)$ for Na_2AgSbX_6 (X = F, Cl, Br, and I)

compound's optical band gap and is found to be extremely near to the calculated electronic energy band gap. This demonstrates the strong correctness of our observations.

Figure 5(c) demonstrates the variation in absorption coefficient $\alpha(\omega)$ of these materials with the incident energy. Any material's absorption coefficient $\alpha(\omega)$ provides information regarding the amount of incident electromagnetic energy that a material's unit thickness has absorbed. For a higher absorption coefficient, a material responds more favorably in the transit of electrons from its valence band to its conduction band. The optical conductivity of a substance can be used to explain how well electrons conduct there when exposed to EM radiation. The spectrum of the examined compounds' optical conductivity with varied EM radiation energy is shown in Fig. 5(d). With increasing frequency of incident radiation, optical conductivity begins to rise for each of these compounds and reaches a noticeably greater value in the visible range of EM radiation. After the visible region, it decreases in the near UV range and further starts to increase and reaches its peak value in the UV region. Figure 5(c) and (d) show that for these compounds, maxima and minima of optical conductivity and absorption coefficient occur in the same region of incident EM radiation; the maximum is observed in the visible region and UV region. It supports the theoretical viewpoint and demonstrates the precision of the suggested results.

An optical parameter relating to the passage of light through the material is the refractive index, denoted by n(ω). It characterizes a material's ability to absorb radiation that comes its way. Na_2AgSbX_6 (X = F, Cl, Br, and I) compounds' static refractive index values, i.e., $n(0)$, are determined to be 1.974, 2.346, 2.637, and 3.040, respectively. The value of $n(0)$ rises with the X-atom's size. We can see from Figs. 5(a) and 6(a) that $n(\omega)$ changes similarly to $\varepsilon_1(\omega)$ with rising incidence energy, but unlike $\varepsilon_1(\omega)$, it never goes negative. This means that the compound is treated as transparent for the high frequency of incident radiation. The damping of oscillations in the electric vector of incident radiation is proportional to a specimen's extinction coefficient $k(\omega)$. Figures 5(a) and 6(b) indicate that $k(\omega)$ has certain peaks that are extremely close to the frequencies where $\varepsilon_1(\omega)$ exhibits valleys or zeros.

The optical reflectivity $R(\omega)$ of these substances is depicted in Fig. 6(c). This graph shows that for Na_2AgSbX_6 (X = F, Cl, Br, and I), the reflectance at zero-frequency $R(0)$ is 54.9%, 47.9%, 59.2%, and 64.1%, respectively. For all substances, the $R(\omega)$ value initially rises steadily in the infrared and near-infrared regions, peaks in the visible range, and then falls to its lowest value in the near-UV region for all substances. Furthermore, it evolves in the UV zone more quickly than elsewhere. For all of these compounds, the UV area has seen the highest value of reflectance. These materials are therefore suitable for photovoltaics in the visible spectrum and can be employed as promising shields for high-energy UV radiation. Figure 6(d) illustrates the material's energy loss function $E_{loss}(\omega)$. It describes the energy dissipation that occurs when an electron travels within a substance. Plasma resonance, or the simultaneous oscillation of valence

band electrons, is characterised by peaks in $E_{loss}(\omega)$'s spectra, and the frequency of incident energy at which plasma resonance occurs is referred to as the plasma frequency (ω_P). According to Fig. 6(d), for these compounds distinct peaks may be detected in the high-energy UV region between 10 and 13 eV. Table 1 lists the static values of various optical properties for these materials, including dielectric constant $\varepsilon_1(0)$, refractive index $n(0)$, and reflectivity $R(0)$.

Thermoelectric properties

Thermoelectric parameters including Seebeck coefficient (S), electrical conductivity (σ), and electronic thermal conductivity (κ_e) have been computed for varying chemical potentials by using the output of structural and electronic parameters as input parameters in the BoltzTraP code [33], and variation in these parameters has been represented graphically in Fig. 7. This code is based on the constant relaxation time approach (CRTA); hence, the σ and κ_e are calculated in terms of relaxation time, while the Seebeck coefficient (S) is calculated autonomously of any adaptable constraint in this constant relaxation time approach (CRTA). As a result, despite measuring the exact value of the power factor ($S^2\sigma$), it is measured in terms of relaxation time ($S^2\sigma/\tau$) had been calculated. The figure of merit of a thermoelectric compound is defined by ZT ($=S^2\sigma T/\kappa$) and used to determine their efficiency, where κ ($=\kappa_e+\kappa_l$) is the total of electron and phonon contributions in thermal conductivity, and T is the absolute temperature; the rest of the symbols have the same meaning as mentioned earlier.

The Seebeck coefficient is a crucial component that reflects the nature of a specimen's dominant charge carriers and is linked with its band structure. Its affirmative and negative values indicate p- and n-type doping in the compound, respectively. The Seebeck coefficient of the studied materials has been determined for diverse chemical potential ($\mu - E_f$) at three varied temperatures (300, 600, and 900 K) and displayed in Fig. 7(a–d). From these figures, we have

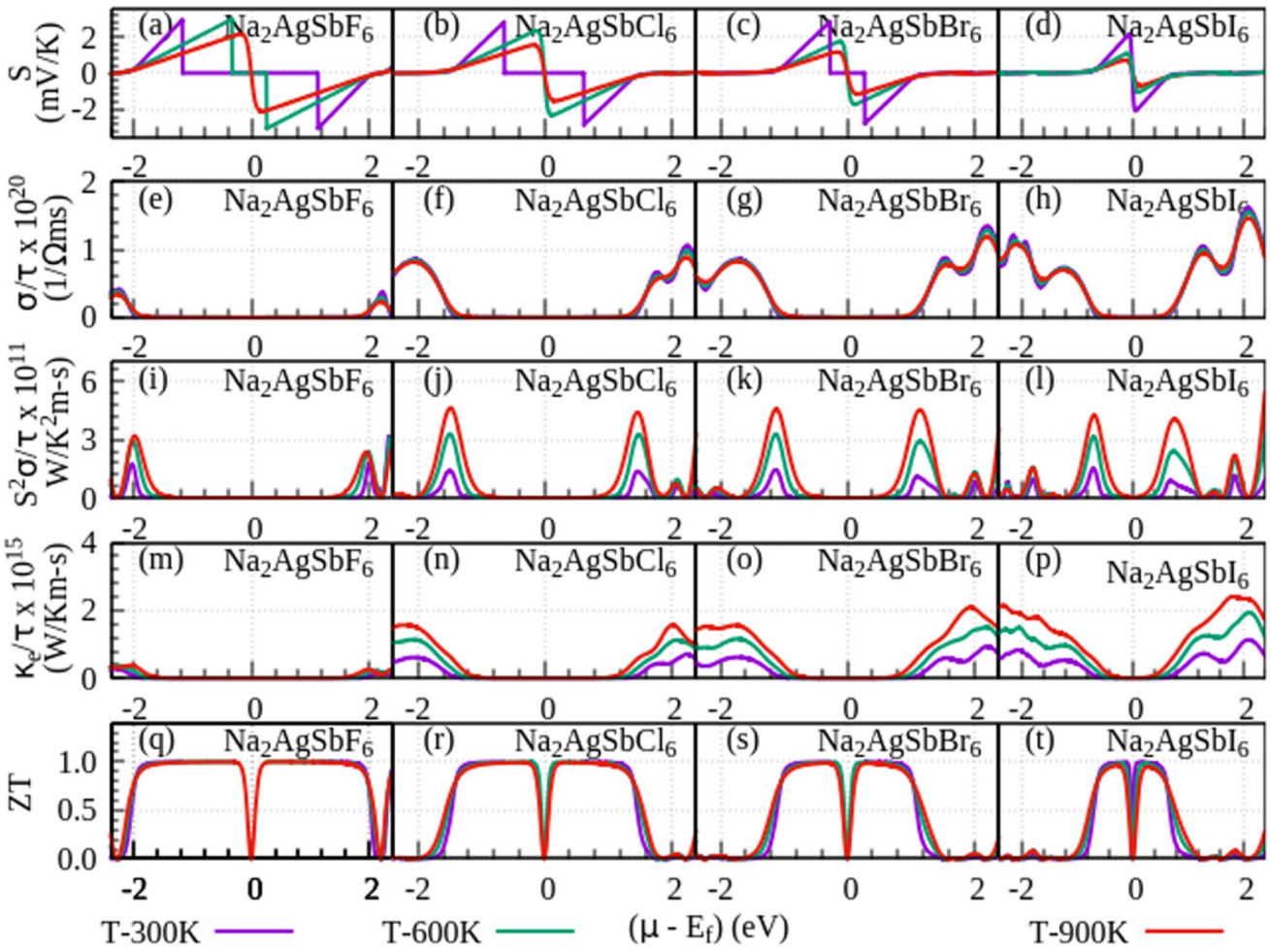

Fig. 7 (**a–d**) Seebeck coefficient (S), (**e–h**) electrical conductivity (σ/τ), (**i–l**) power factor ($S^2\sigma/\tau$), (**m–p**) electronic part of thermal conductivity (κ_e/τ), and (**q–t**) figure of merit (ZT) for Na_2AgSbX_6 (X = F, Cl, Br, and I)

observed that the Seebeck coefficient consists of two peaks, one for each *p*- and *n*-region. We also observed that for all of these compounds, in the proximity of the mid of the band gap, the Seebeck coefficient is higher in the *p*-region compared to the *n*-region and significantly reduces as temperature increases, indicating that at high temperatures; it will behave like a decay factor for the thermoelectric efficiency. It also decreases with the increasing size of the X-atom, which may be understood by the trend of their energy band gap. Because these minima and maxima are located within a very narrow range of the chemical potential, they can be obtained with very low doping concentrations. Aside from this range, the Seebeck coefficient quickly decreases for higher doping concentrations. At 300 and 900 K, the calculated maximum values of S in *p*- and *n*-regions of these compounds have been listed in Table 2.

In Fig. 7(e–h), we have presented the variation in electrical conductivity (σ/τ) for chemical potential ($\mu - E_f$) at three diverse temperatures (300, 600, and 900 K). Unlike the Seebeck coefficient, σ/τ behaves similarly at all temperatures. The increasing chemical potential improves the charge carrier mobility and hence the electrical conductivity, which is verified by these figures. For Na_2AgSbF_6 and Na_2AgSbI_6, for the considered range of chemical potential, the electrical conductivity is higher for the *p*-type configuration, whereas for $Na_2AgSbCl_6$ and $Na_2AgSbBr_6$, it shows the opposite behavior. At 300 and 900 K, the values of σ/τ for the overall range of chemical potential are presented in Table 2.

With the support of the abovementioned thermoelectric parameters, we have assessed the power factor (P.F.) in units of the relaxation time ($S^2\sigma/\tau$). Figure 7(i–l) illustrate the deviation in P.F. concerning chemical potential ($\mu - E_f$). The minimum value of the power factor can be attained when ($\mu - E_f$) lies close to the mid of the energy band gap as the Seebeck coefficient obtains negligible value in the mid of the band gap, and σ/τ (electrical conductivity) is trivial due to very low carrier concentration. Furthermore, as ($\mu - E_f$) rises, both *S* and σ/τ rise with it. A further increase in chemical potential results in a rapid decrease in *S*; however, σ/τ keeps rising. As a result, two distinct peaks are formed in these compounds, for the *p*- and *n*-region separately. From these figures, we observe that the P.F. of all the investigated materials increases with increasing temperature and at any particular temperature P.F. is higher in the *p*-region compared to the *n*-region. Table 2 shows the power factor values for the *p*- and *n*-regions at 300 and 900 K. The theoretical study specifies a narrow range of carrier concentrations for which the power factor is supreme. The optimal carrier concentration to achieve the highest power factor has been demonstrated at 300 and 900 K. The proposed optimal carrier concentration offers a small window for experimental experts to fabricate high-thermoelectric-efficiency materials.

The electronic thermal conductivity (κ_e/τ) has been determined at three different temperatures (300, 600, and 900 K) for the chemical potential ($\mu - E_f$), and these results have been presented in Fig. 7(m–p). To attain supreme thermoelectric efficiency, κ_e/τ needs to be the lowest. From these figures, it has been observed that in both the *p*- and *n*-regions, κ_e rises with rising temperatures. Thus, the lowest value of κ_e/τ can be obtained at 300 K. From these figures, we see that κ_e/τ is the lowest in the region in which the Seebeck coefficient is maximum; hence, in this region, the explored materials will have maximum efficiency. With varying chemical potentials, κ_e/τ follows the same pattern as σ/τ, that is, it rises with growing values of chemical potential but with a smaller factor than σ/τ. In contrast to σ/τ, for a specific value of chemical potential, κ_e/τ has different values at different temperatures. Figure 7(m–p) demonstrate that like σ/τ, for a wide temperature range and considered range of chemical potential, for Na_2AgSbF_6 and Na_2AgSbI_6, the electronic thermal conductivity is higher for the *p*-type

Table 2 Thermoelectric parameters: Seebeck coefficient (*S*); electrical conductivity per unit relaxation time (σ/τ); electronic thermal conductivity per unit relaxation time (κ_e/τ); power factor per unit relaxation time ($S^2\sigma/\tau$); optimal carrier concentration per unit cell for maximum P.F. (N); and figure of merit ($ZT = S^2\sigma T/\kappa_{total}$) of Na_2AgSbX_6 (X = F, Cl, Br, and I)

Compounds		*S* (mV/K)		σ/τ (10^{20}/Ω ms)		κ_e/τ (10^{15} W/K ms)		P. F. (10^{11} W/K^2 ms)		*N* (carriers/u.c.)		*ZT*	
		300 K	900 K	300 K	900 K	300 K	900 K	300 K	900 K	300 K	900 K	300 K	900 K
Na_2AgSbF_6	p-type	2.911	2.132	0.411	0.333	0.280	0.380	1.715	3.183	0.085	0.144	0.998	0.997
	n-type	−3.031	−2.109	0.371	0.224	0.205	0.263	1.785	2.348	−0.179	−0.429	0.999	0.998
$Na_2AgSbCl_6$	p-type	2.795	1.537	0.853	0.813	0.611	1.562	1.386	4.619	0.075	0.114	0.998	0.992
	n-type	−2.833	−1.535	1.056	0.882	0.706	1.570	1.361	4.401	−0.058	−0.142	0.998	0.992
$Na_2AgSbBr_6$	p-type	2.802	1.152	0.854	0.821	0.617	1.555	1.429	4.566	0.066	0.112	0.998	0.984
	n-type	−2.768	−1.146	1.343	1.184	0.932	2.088	1.101	4.523	−0.034	−0.121	0.998	0.983
Na_2AgSbI_6	p-type	2.097	0.710	1.204	1.072	0.834	2.139	1.521	4.252	0.061	0.111	0.994	0.959
	n-type	−2.058	−0.693	1.612	1.461	1.129	2.406	0.883	4.060	−0.022	−0.098	0.994	0.946

configuration, whereas for $Na_2AgSbCl_6$ and $Na_2AgSbBr_6$, it is higher for the *n*-type configuration. At 300 and 900 K, the highest value of κ_e/τ for all the investigated compounds in both regions has been listed in Table 2.

The efficiency of thermoelectric substances can be determined using the figure of merit ($ZT = S^2\sigma T/\kappa$). Based on the above-discussed transport parameters, ZT of Na_2AgSbX_6 (X = F, Cl, Br, and I) compounds at three temperatures of 300, 600, and 900 K has been determined. A lower value of thermal conductivity and a greater value of power factor is required to gain a higher figure of merit. Though no theoretical limit is set to gain the maximum value of the figure of merit, hence based on the combination of these three transport parameters (S, σ, and κ), reaching higher values of ZT remain a challenge. As a result, to raise the figure of merit (ZT), there must be an agreement among such varying factors. Figure 7(q–t) demonstrate the deviation in ZT as a function of chemical potential. At 300 and 900 K, the supreme value of ZT for *p*- and *n*-regions are given in Table 2. From these figures and Table 2, it is evident that in these compounds show ZT ≈ 1 at 300 K and a small decrease in ZT is observed with increasing temperature. Besides this, at 300 K, the ZT of these materials (except Na_2AgSbI_6) is similar in both *p*- and *n*-regions, while for Na_2AgSbF_6, it is a bit higher in the *n*-region compared to the *p*-region. It validates that these materials are best not only at lower temperatures but at high temperatures also. We see that among all the explored compounds, Na_2AgSbI_6 shows the least performance. Soni et al. [41] have computed the ZT of a similar family of the halide double perovskite materials Cs_2ZSbX_6 (Z = Ag, Cy; X = Cl, Br, I), which was found to be nearly 0.85 for n- and p-regions. It confirms that the investigated ZT of the titled materials is far better in comparison of ZT of Cs_2ZSbX_6 (Z = Ag, Cy; X = Cl, Br, I) materials.

Thermodynamic properties

The quasi harmonic Debye approximation model, as implemented in the Gibbs2 package, has been used to estimate the thermodynamic characteristics of the examined material Ra_2LaNbO_6 concerning variations in temperature (T) and pressure (P) [34, 45]. Plots of the thermodynamic parameters (Fig. 8) for the temperature range of 0–1000 K and the pressure range of 0–10 GPa are presented in this study. Figure 8(a–d) illustrate how the bulk modulus (B) changes when temperature and pressure change within the previously specified regulated range. According to Fig. 8(a–d), the examined compound's bulk modulus (B) is observed to decline monotonically with increasing temperature, but it rises as the pressure builds and reaches its highest point. at 0 K for a fixed pressure. Any material's bulk modulus (B) can be used to define its hardness under pressure. Therefore, the decline in B indicates that material hardness reduces as temperature rises. Figure 8(e–h) show the variation of Debye temperature (θ_D) of Ra_2LaNbO_6 with varying temperatures and pressures, respectively. θ_D is strongly related to the compound's distinct physical characteristics (such as elastic constant, thermal expansion). Figure 8(e–h) show that θ_D appears to decrease as temperature rises. It is discovered that θ_D has a greater value for the low temperature at a constant pressure. At constant temperature, θ_D is appeared to rise with increasing pressure. Entropy (S) is an important parameter and as illustrated in Fig. 8(i–l), it is zero at zero kelvin and increases as temperature rises. It is also observed that S decreases with increasing pressure. Entropy is a measure of how disorderly a system is, and since S increases with temperature, the compound becomes more random [46]. This might be because the system produces more thermal energy in proportion to temperature, which causes the system to vibrate more. The increase in the entropy value results from these vibrational (anharmonic) motions. The fluctuation in specific heat (C_p and C_v) concerning temperature and pressure is shown in Fig. 8(m–p) and (q–t), respectively. It is discovered that C_p and C_v rise as the temperature rises. It can be interpreted that at low temperatures (below ~ 300 K), C_p and C_v obey the T^3 law and are consistent with the well-known Dulong–Petit law [47], while at high temperatures, C_p grows with temperature, and due to suppression of an anharmonic consequence C_v becomes constant. The value at which C_v becomes constant is referred to as the Dulong-Petit limit. It is clear from Fig. 8(q–t) that the Dulong-Petit limit of Na_2AgSbX_6 (X = F, Cl, Br, and I) compounds upsurges for the growing size of X-atom.

Mechanical and phonon stability

To understand the mechanical performance of the investigated materials, we have calculated their elastic parameters using the IRElast package in WIEN2k. Na_2AgSbX_6 (X = F, Cl, Br, and I) displays its cubic crystal structure; therefore, their mechanical characteristics may be calculated using only the C_{11}, C_{12}, and C_{44} elastic constants [48]. These elastic constants can be used to calculate additional elastic parameters, including the bulk modulus (B), shear modulus (G), Young's modulus (Y), Poisson's ratio (η), Zener anisotropy factor (A_Z), etc. [48]. Our findings for the investigated halide double perovskites' elastic characteristics are displayed in Table 3. For Na_2AgSbF_6 and Na_2AgSbI_6, elastic constants C_{11}, C_{12}, and C_{44} obey the Born-Huang stability criteria [49], which include "$C_{11} - C_{12} > 0$, $C_{11} > 0$, $C_{44} > 0$, and $C_{11} + 2C_{12} > 0$", whereas for $Na_2AgSbCl_6$ and $Na_2AgSbBr_6$, $C_{11} - C_{12} < 0$, which shows the less mechanical stability of these two materials. The strength of a material under pressure is indicated by the high values of its bulk modulus. For the investigated compounds, bulk modulus in Table 3 is in best agreement with that in Table 1, which

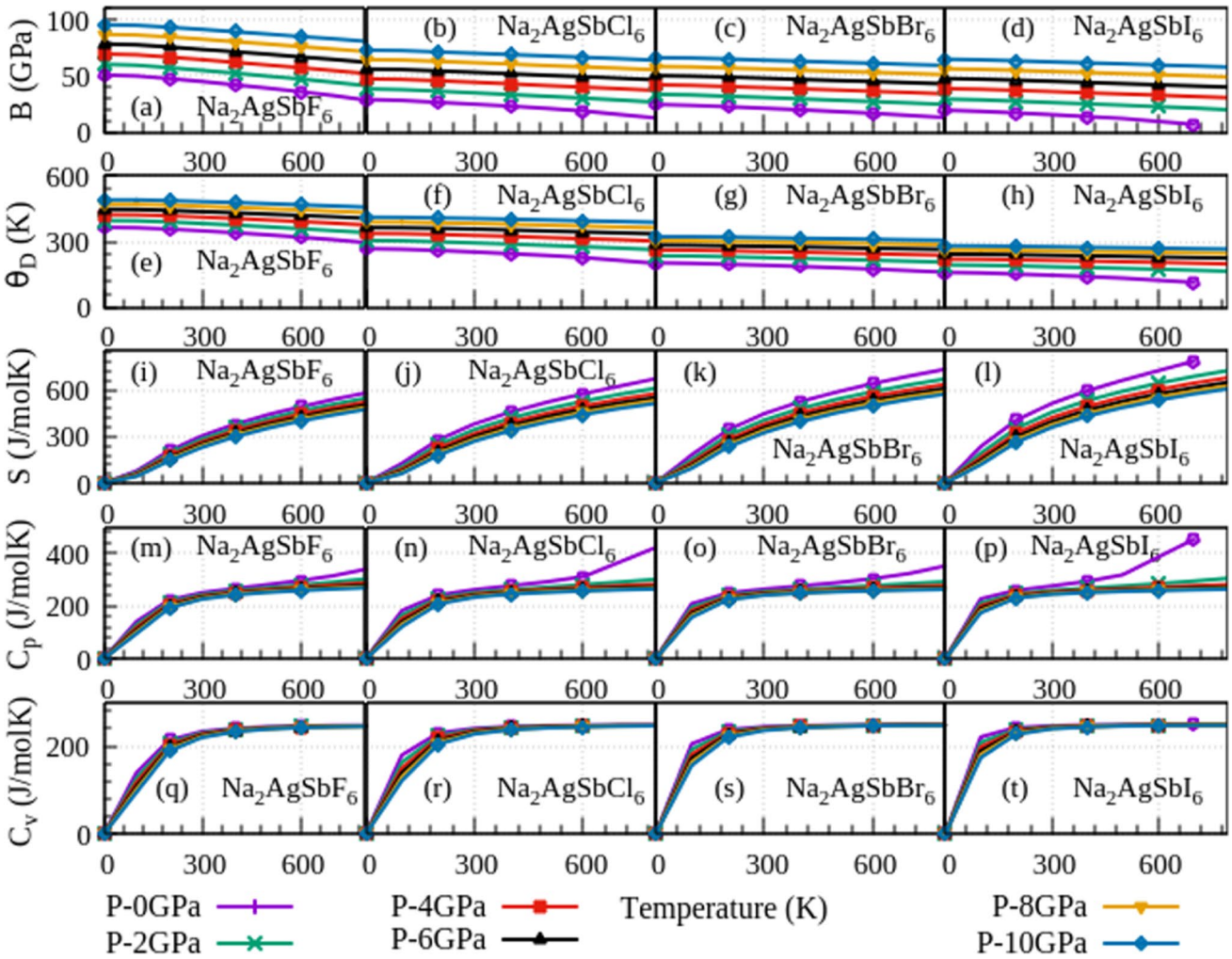

Fig. 8 (**a–d**) Bulk modulus (*B*), (**e–h**) Debye temperature (θ_D), (**i–l**) entropy (*S*), (**m–p**) specific heat at constant pressure (C_p), and (**q–t**) specific heat at constant volume (C_v) for Na_2AgSbX_6 (X = F, Cl, Br, and I)

shows the accuracy of our calculations. Shape deformation brought about by a material is defined by its shear modulus (*G*). The titled materials have a substantially less plastic twist, as indicated by their relatively smaller shear modulus. Young's modulus is a measure of a material's stiffness, and materials with high values show better resistance to deformation. Therefore, it is anticipated that the studied compounds' calculated Young's modulus will demonstrate its rigidity.

In order to determine if the titled compounds are ductile or brittle, Pugh's ratio (*B*/*G*) was determined. Materials are regarded as ductile if their *B*/*G* ratio is more than 1.75; otherwise, they are brittle [50]. Na_2AgSbX_6 (X = F, Cl, Br, and I) have a *B*/*G* ratio of > 1.75, which highlights their ductile nature. The relation $C_p = C_{12} - C_{44}$ [51], which defines Cauchy pressure, reveals the kind of bonds. A negative Cauchy pressure indicates that covalent bonds predominate, whereas a positive value indicates that ionic

Table 3 Computed elastic parameters of Na_2AgSbX_6 (X = F, Cl, Br, and I) under ambient conditions

Elastic parameters (PBE-GGA)	Na_2AgSbF_6	$Na_2AgSbCl_6$	$Na_2AgSbBr_6$	Na_2AgSbI_6
C_{11} (GPa)	125.16	6.62	3.32	41.42
C_{12} (GPa)	15.29	39.43	41.66	8.98
C_{44} (GPa)	2.814	5.37	3.95	3.86
B (GPa)	51.91	28.49, 32.9[a]	28.88, 28.11[a]	19.80, 23.01[a]
G (GPa)	14.09	4.06, 14.16[a]	1.17, 13.1[a]	7.17, 10.52[a]
Y (GPa)	38.78	11.65, 37.16[a]	3.46, 34.02[a]	19.21, 27.35[a]
B/*G*	3.68	7.00, 2.32[a]	24.68, 2.14[a]	2.75, 2.19[a]
C_p (GPa)	12.47	34.05	37.71	5.12
η	0.376	0.432	0.480	0.338
A_Z	0.051	−0.328	−0.206	0.238

[a]Reference [41] for Cs_2AgSbX_6 (X = Cl, Br, I)

Table 4 The calculated values for Na_2AgSbX_6 (X = F, Cl, Br, and I) halide double perovskite material's density (in kg/m^3), Debye temperature (in K), ν_l, ν_t, and ν_m (in m/s)

Parameters	Na_2AgSbF_6	$Na_2AgSbCl_6$	$Na_2AgSbBr_6$	Na_2AgSbI_6
ρ	871.098	671.684	894.337	99.957
v_l	9009.788	7106.606	5834.795	17,142.077
v_t	4023.071	2461.041	1143.962	8474.883
v_m	4538.894	2797.954	1307.869	9513.453
θ_D	321.439	168.522	74.945	508.952

bonds predominate in the same substance. Positive Cauchy pressure of the investigated materials justifies greater dominance of ionic bonds. Similar to Pugh's ratio, Poisson's ratio (η) can divide crystalline materials into brittle and ductile groups. This classification has a separation line of $\eta = 0.26$. Below this line, brittle materials are located, and above it, ductile materials are located [52]. The calculated value of η for Na_2AgSbX_6 (X = F, Cl, Br, I) crystals is more than 0.26, as given in Table 2. Therefore, Poisson's ratio and Pugh's ratio both anticipated the same outcomes (ductile material) for the investigated halide perovskite materials. Poisson's ratio also evaluates the resistance of crystals to shearing. Its lower Poisson's ratio value indicates its resilience against shearing. When subjected to a central or non-central force, a solid material exhibits stability. The type of force that maintains the stability of a solid material can also be predicted from Poisson's ratio. A solid that exhibits a Poisson's ratio between 0.25 and 0.50 is referred to as a central force solid and is thought to be stabilized by the central force. The term "non-central force solid" refers to a solid that is stabilized by non-central force and has a Poisson's ratio outside of this range [53]. The Poisson's ratio for Na_2AgSbX_6 (X = F, Cl, Br, I) materials lies in the range from 0.376 to 0.338, indicating that these are central force solids. Similar to this, materials with a Zener anisotropic factor of $A_Z = 1$ are regarded as being isotropic [48]. The amount of deviance from unity is used to gauge the degree of elastic anisotropy. The investigated materials are confirmed in Table 2 to be anisotropic double perovskite compounds.

The average velocity, $v_m = \left[\frac{1}{3}\left(\frac{2}{v_t^3} + \frac{1}{v_l^3}\right)\right]^{-1/3}$, is obtained from the expression of longitudinal ($v_l = \sqrt{\frac{3B+4G}{3\rho}}$) and transverse velocities ($v_t = \sqrt{\frac{G}{\rho}}$), whereas the Debye temperature, ($\theta_D = \frac{h}{k}\left[\left(\frac{3n}{4\pi}\right)\left(\frac{N_A\rho}{M}\right)\right]^{1/3} v_m$), is an approximation of the greatest attainable temperature for a crystal's normal modes of vibration. It is also a crucial characteristic of materials because it links their elastic characteristics to thermodynamic characteristics like melting point, specific heat, and entropy. The Plank's constant, Boltzmann constant, Avogadro's number, density, and average sound velocity are all denoted by the symbols h, k, N_A, ρ, and v_m in the expression of θ_D. Table 4 contains the computed results for the aforementioned parameters. The table shows that the Debye temperature for Na_2AgSbX_6 (X = F, Cl, Br, and I) is calculated to be 321.439, 168.522, 74.945, and 508.952 K, respectively. The Debye temperature can be used to determine a solid's Debye hardness [54, 55], i.e., Na_2AgSbF_6 and Na_2AgSbI_6 exhibit high Debye hardness, whereas $Na_2AgSbCl_6$ and $Na_2AgSbBr_6$ exhibit comparatively low Debye hardness as shown in Table 4. A comparison of the mechanical parameters of the titled materials with a family of similar materials has been shown in Table 1.

We have performed phonon lattice dynamics within harmonic approximation to investigate the dynamical stability of the subject line halide double perovskite

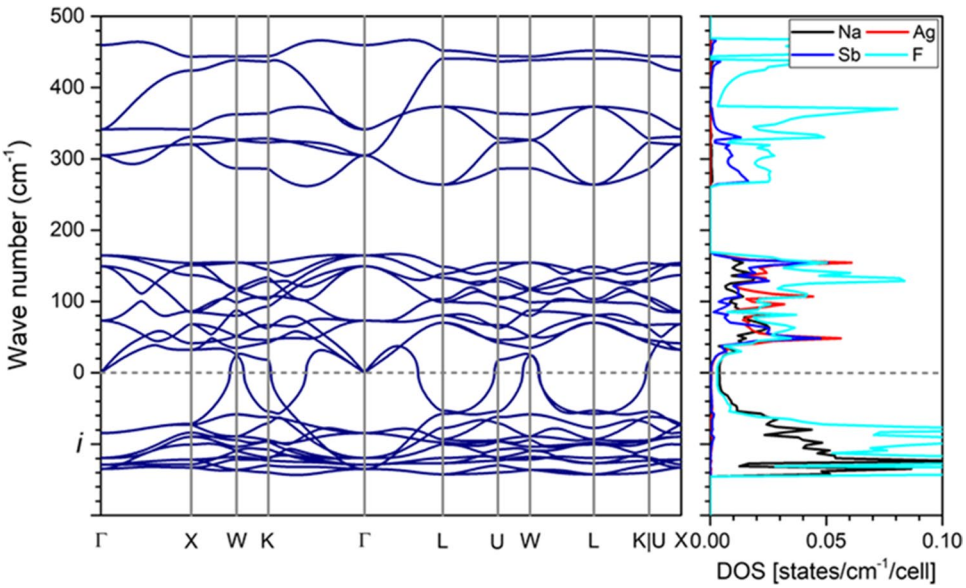

Fig. 9 The computed phonon dispersion spectra along with atom-projected phonon density of states of Na_2AgSbF_6 ($Fm\bar{3}m$; SG no. 225)

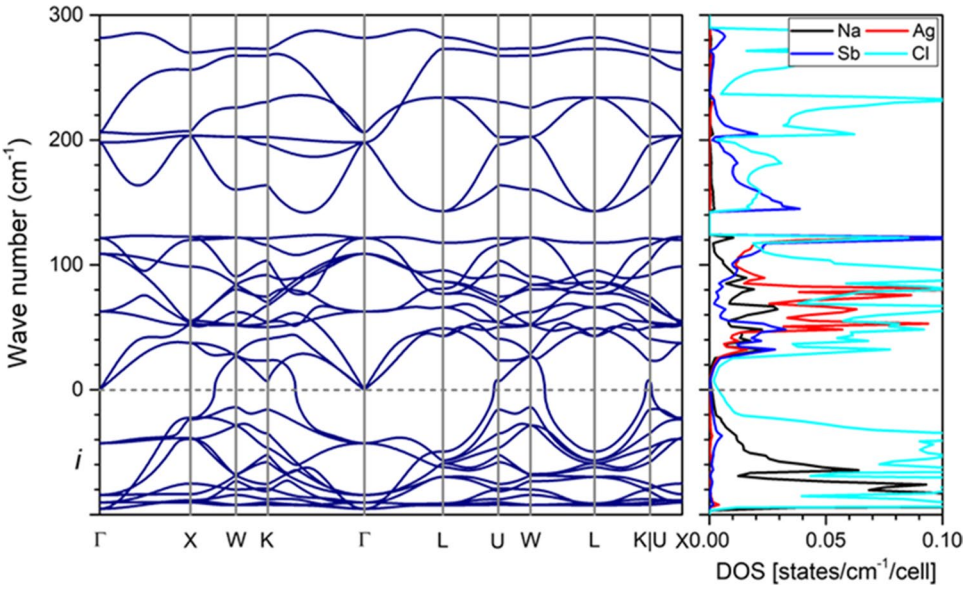

Fig. 10 The computed phonon dispersion spectra along with atom-projected phonon density of states of $Na_2AgSbCl_6$ ($Fm\bar{3}m$; SG no. 225)

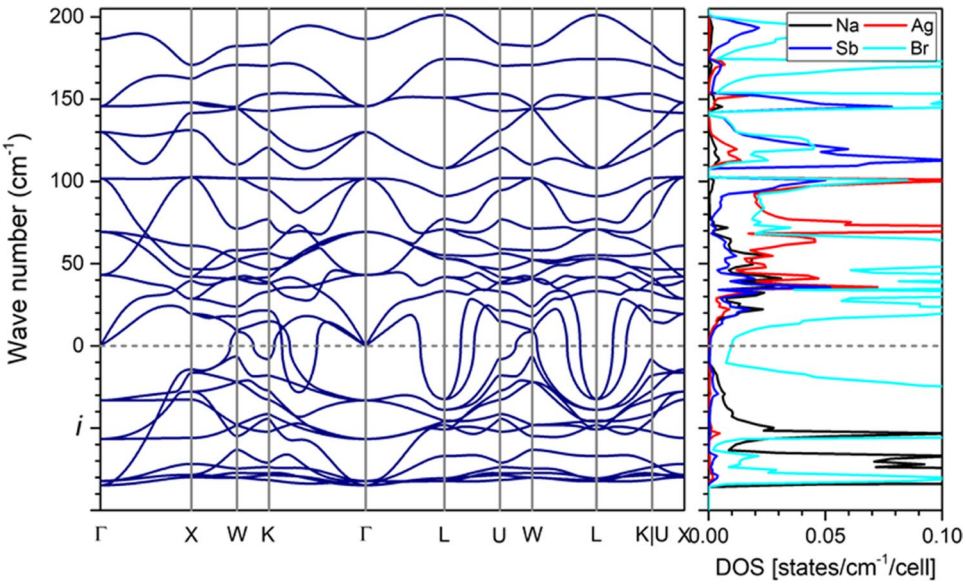

Fig. 11 The computed phonon dispersion spectra along with atom-projected phonon density of states of $Na_2AgSbBr_6$ ($Fm\bar{3}m$; SG no. 225)

(Na_2AgSbX_6) systems. All the subject line compositions are dynamically unstable; they show the presence of imaginary phonon modes throughout the Brillouin zone. The corresponding phonon dispersion spectra, along with atom-projected phonon density of states of all the compositions, is shown in Figs. 9, 10, 11, and 12. The presence of imaginary phonon modes in the perovskite systems is not uncommon. It has been observed in the literature that the presence of imaginary phonon modes in the perovskite system does not hinder its experimental realization. For example, among the four experimentally known phases of $BaCeO_3$ [56–59], only its ground-state (lowest temperature) phase, i.e., *Pnma* (space group no. 62), shows dynamic stability, and the rest of the phases possess imaginary phonon modes [60, 61]. Similarly, although known experimentally, the high-temperature alpha (α) and beta (β) phases of $CsSnI_3$ also show dynamical instability [62–64]. The examples as mentioned above are to name a few; often, such modes are related to the structural phase transition among perovskite materials [60, 65–70]. Hence, a further experimental study should be initiated to explore these materials.

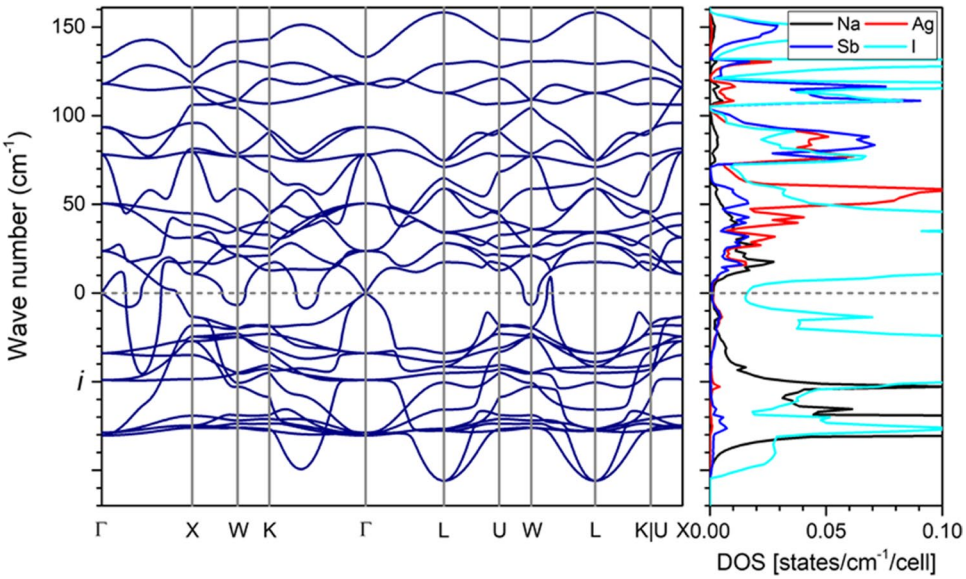

Fig. 12 The computed phonon dispersion spectra along with atom-projected phonon density of states of Na_2AgSbI_6 ($Fm\bar{3}m$; SG no. 225)

Conclusion

In the ab initio study of Na_2AgSbX_6 (X = F, Cl, Br, I) compounds, we found that their lattice constant lies between 9.056 and 11.988 Å. They have an indirect band gap in the range of 1.273–3.986 eV. From the detailed explanation of optical characteristics, it can be concluded that all four materials are most suitable for photovoltaic applications in the visible and UV range. All the titled compounds show a high figure of merit (ZT≈1) in both *p*- and *n*-regions at all the considered temperatures. A slight decrease in ZT has also been observed with increasing temperature. Thus, we recommend these materials of utmost use in TE devices also. All the subject line materials are found thermodynamically stable. Among these halide double perovskite materials, Na_2AgSbF_6 and Na_2AgSbI_6 show mechanically stable, whereas $Na_2AgSbCl_6$ and $Na_2AgSbBr_6$ do not satisfy all criteria of mechanical stability. From phonon computation, it is observed that all the studied materials do not show dynamical stability but based on the promising properties shown by the systems under this study for green energy technology, we strongly believe that their dynamical and mechanical instability can be overlooked positively, and further experimental study should be initiated to explore these materials.

Author contribution Sunita Kumari**:** Investigation, writing original draft; Peeyush Kumar Kamlesh: methodology; Lalit Kumari: data curation; Sudhir Kumar: software; Sarita Kumari: supervision; Rashmi Singh: visualization; Rajeev Gupta: conceptualization; Manendra S. Chauhan: validation; Upasana Rani: resources; Ajay Singh Verma: writing—reviewing and editing.

Data availability Data and materials will be available on reasonable request.

Declarations

Competing interests The authors declare no competing interests.

Ethical approval Not applicable on this work.

Conflict of interest This manuscript does not include conflict of interest.

References

1. Xiao Z, Yan Y (2017) Progress in theoretical study of metal halide perovskite solar cell materials. Adv Energy Mater 7:1701136
2. Lai X, Li W, Gu X, Chen H, Zhang Y, Li G, ... Sun XW (2022) High-performance quasi-2D perovskite solar cells with power conversion efficiency over 20% fabricated in humidity-controlled ambient air. Chem Eng J 427:130949
3. Rani U, Kamlesh PK, Shukla A, Verma AS (2021) Emerging potential antiperovskite materials ANX_3 (A= P, As, Sb, Bi; X= Sr, Ca, Mg) for thermoelectric renewable energy generators. J Solid State Chem 300:122246
4. Rani U, Soni Y, Kamlesh PK, Shukla A, Verma AS (2021) Fundamental theoretical design of Na-ion and K-ion based double antiperovskite X_6SOA_2 (X= Na, K; A= Cl, Br and I) halides: potential candidate for energy storage and harvester. Int J Energy Res 45:13442–13460
5. Rani U, Kamlesh PK, Agarwal R, Kumari J, Verma AS (2021) Electronic and thermo-physical properties of double antiperovskites X_6SOA_2 (X= Na, K and A= Cl, Br, I): a non-toxic and efficient energy storage materials. Int J Quantum Chem 121:e26759
6. Rani U, Kamlesh PK, Agrawal R, Shukla A, Verma AS (2022) Emerging study on lead-free hybrid double perovskite (CH3NH3)2AgInBr 6: potential material for energy conversion between heat and electricity. Energy Technol 2200002
7. Liu S, Chen R, Tian X, Yang Z, Zhou J, Ren F ... Chen W (2022) Boost the efficiency of nickel oxide-based formamidinium-cesium perovskite solar cells to 21% by using coumarin 343 dye as defect passivator. Nano Energy 94:106935

8. Cheng L, Xu B, Li X, Zeng Y, Meng L (2022) Electronic and photovoltaic properties of superlattices constructed by organic–inorganic perovskites: a theoretical perspective. ACS Appl Energy Mater 5:2430–2441
9. Tailor NK, Listorti A, Colella S, Satapathi S (2022) Lead-free halide double perovskites: fundamentals, challenges, and photovoltaics applications. Adv Mater Technol 2200442. https://doi.org/10.1002/admt.202200442
10. Li Q, Wang Y, Pan W, Yang W, Zou B, Tang J, Quan Z (2017) High-pressure band-gap engineering in lead-free $Cs_2AgBiBr_6$ double perovskite. Angew Chem Int Ed 56:15969–15973
11. Yadav SC, Srivastava A, Manjunath V, Kanwade A, Devan RS, Shirage PM (2022) Properties, performance and multidimensional applications of stable lead-free $Cs_2AgBiBr_6$ double perovskite. Mater Today Phys 26:100731
12. Pantaler M, Fettkenhauer C, Nguyen HL, Anusca I, Lupascu DC (2018) Deposition routes of $Cs_2AgBiBr_6$ double perovskites for photovoltaic applications. MRS Adv 3:1819–1823
13. Al-Qaisi S, Mebed AM, Mushtaq M, Rai DP, Alrebdi TA, Sheikh RA, Rached H et al (2023) A theoretical investigation of the lead-free double perovskites halides Rb2XCl6 (X= Se, Ti) for optoelectronic and thermoelectric applications. J Comput Chem. https://doi.org/10.1002/jcc.27119
14. Mebed AM, Al-Qaisi S, Azmat Ali M (2022) Study of optoelectronic and thermoelectric properties of double perovskites Rb_2AgBiX_6 (X= Br, I): by DFT approach. Eur Phys J Plus 137:1–8
15. Al-Qaisi S, Mahmood Q, Kattan NA, Alhassan S, Alshahrani T, Sfina N, Brini S, Hakamy A, Mera A, Amin MA (2023) Tuning of band gap by variation of halide ions in K_2CuSbX_6 (X= Cl, Br, I) for solar cells and thermoelectric applications. J Phys Chem Solids 174:111184
16. Albalawi H, Nazir G, Younas M, Al-Qaisi S, Ashiq MGB, Alzahrani J, Somaily HH, Morsi M, Ghrib T (2022) Study of lead-free vacancy ordered double perovskites Cs_2TeX_6 (X= Cl, Br, I) for solar cells, and renewable energy. Phys Scr 97:095801
17. Ali MA, Alshgari RA, Bahajjaj AAA, Sillanpää M (2023) The study of new double perovskites K_2AgAsX_6 (X= Cl, Br) for energy-based applications. J Taibah Univ Sci 17:2170680
18. Ullah R, Ali MA, Khan A, Alshgari RA, Mushab MSS, Samad A (2022) Effect of cation exchange on structural, electronic, magnetic and transport properties of Ba_2MReO_6 (M= In, Gd). J Magn Magn Mater 546:168816
19. Ullah R, Ali MA, UlHaq B, Khan A, Mahmood Q, Murtaza G (2022) Exploring electronic, structural, magnetic and thermoelectric properties of novel Ba_2EuMoO_6 double perovskite. Mater Sci Semicond Process 137:106218
20. Zhang X, Lv Y, Lv Y, Liu Y, Yang Z (2022) Indirect-to-direct band gap transition and optical properties of Cs_2BiAgX_6 with mechanical strains: the density functional theory investigation. J Market Res 17:425–432
21. Muscarella LA, Hutter EM (2022) Halide double-perovskite semiconductors beyond photovoltaics. ACS Energy Lett 7:2128–2135
22. Zhang Z, Sun Q, Lu Y, Lu F, Mu X, Wei SH, Sui M (2022) Hydrogenated $Cs_2AgBiBr_6$ for significantly improved efficiency of lead-free inorganic double perovskite solar cell. Nat Commun 13:1–12
23. Abdelsamie MA, Cruse K, Tamura N, Ceder G, Sutter-Fella CM (2022) Impact of processing conditions on the film formation of lead-free halide double perovskite $Cs_2AgBiBr_6$. J Mater Chem A. https://doi.org/10.1039/D2TA00763K
24. Amraoui S, Feraoun A, Kerouad M (2022) Performance analysis of lead-free halide double perovskite-based photovoltaic devices for solar cell conception. J Alloys Compd 166509. https://doi.org/10.1016/j.jallcom.2022.166509
25. Al-Qaisi S, Mushtaq M, Alomairy S, Vu TV, Rached H, Haq BU, Mahmood Q, Al-Buriahi MS (2022) First-principles investigations of Na_2CuMCl_6 (M= Bi, Sb) double perovskite semiconductors: materials for green technology. Mater Sci Semicond Process 150:106947
26. Asghar M, Zanib M, Khan MA, Niaz S, Noor NA, Dahshan A (2022) Tuning of the bandgap of Rb_2ScAgX_6 (X= Cl, Br, I) double perovskites through halide ion replacement for solar cell applications. Mater Sci Semicond Process 148:106819
27. Dar SA, Want B, Khandy SA (2022) Computer based predictions of structural stability and systematic study of magneto-electronic and optical properties of lead free halide double perovskites: Cs_2KXCl_6: X= Co and Ni. J Magn Magn Mater 545:168603
28. Nawaz PA, Mustafa GM, Iqbal SS, Noor NA, Ahmad TS, Mahmood A, Neffati R (2022) Theoretical investigations of optoelectronic and transport properties of Rb_2YInX_6 (X= Cl, Br, I) double perovskite materials for solar cell applications. Sol Energy 231:586–592
29. Zheng Y, Luo F, Ruan L, Tong J, Yan L, Sun C, Zhang X (2022) A facile fabrication of lead-free Cs2NaBiI6 double perovskite films for memory device application. J Alloy Compd 909:164613
30. Kibbou M, Haman Z, Khossossi N, Singh D, Essaoudi I, Ainane A, Ahuja R (2022) Probing the electronic, optical and transport properties of halide double perovskites $Rb_2InSb(Cl, Br)_6$ for solar cells and thermoelectric applications. J Solid State Chem 312:123262
31. Blaha P, Schwarz K, Madsen G, Kvasnicka D, Luitz J (2001) WIEN2K, an augmented plane wave + local orbital program for calculating crystal properties. Austria Karlheinz Schwarz, Technical University, Wien
32. Perdew JP, Burke K, Ernzerhof M (1996) Generalized gradient approximation made simple. Phys Rev Lett 77:3865–3868
33 Madsen GKH, Singh DJ (2006) BoltzTraP. A code for calculating band–structure-dependent quantities. Comput Phys Commun 175:67–71
34. Otero-de-la-Roza A, Abbasi-Pérez D, Luaña V (2011) Gibbs2: a new version of the quasiharmonic model code. II. Models for solid-state thermodynamics, features and implementation. Comput Phys Commun 182:2232–2248
35. Blöchl PE (1994) Projector augmented-wave method. Phys Rev B 50:17953–17979
36. Kresse G, Joubert D (1999) From ultrasoft pseudopotentials to the projector augmented-wave method. Phys Rev B 59:1758–1775
37. Kresse G, Furthmüller J (1996) Efficient iterative schemes for ab initio total-energy calculations using a plane-wave basis set. Phys Rev B 54:11169–11186
38. Togo A, Oba F, Tanaka I (2008) First-principles calculations of the ferroelastic transition between rutile-type and $CaCl_2$-type SiO_2 at high pressures. Phys Rev B 78:134106
39. Parlinski K, Li ZQ, Kawazoe Y (1997) First-principles determination of the soft mode in cubic ZrO_2. Phys Rev Lett 78:4063–4066
40. Kamlesh PK, Gautam R, Kumari S, Verma AS (2021) Investigation of inherent properties of XScZ (X = Li, Na, K; Z = C, Si, Ge) half-Heusler compounds: appropriate for photovoltaic and thermoelectric applications. Physica B Condens Matter 615:412536
41. Soni Y, Rani U, Shukla A, Joshi TK, Verma AS (2022) Transition metal-based halides double Cs2ZSbX6 (Z= Ag, Cu, and X= Cl, Br, I) perovskites: a mechanically stable and highly absorptive materials for photovoltaic devices. J Solid State Chem 314:123420
42. Kamlesh PK, Agarwal R, Rani U, Verma AS (2021) First-principles calculations of inherent properties of Rb based state-of-the-art half-Heusler compounds: promising materials for renewable energy applications. Phys Scr 96:115802
43. Verma P, Singh C, Kamlesh PK, Kaur K, Verma AS (2023) Nowotny-Juza phase KBeX (X= N, P, As, Sb, and Bi) half-Heusler compounds: applicability in photovoltaics and thermoelectric generators. J Mol Model 29:23

44. Kamlesh PK, Pravesh, Kumari S, Verma AS (2020) Effect of hybrid density functionals on half-Heusler LiZnX (X = N, P and As) semiconductors: potential materials for photovoltaic and thermoelectric applications. Phys Scr 95:095806
45. Kumar A, Kumar M, Singh RP (2021) Magnetic, opto-electronic, and thermodynamic properties of half-metallic double perovskite oxide, Ba_2YbTaO_6: a density functional theory study. J Mater Sci: Mater Electron 32:12951–12965
46. Francisco E, Recio J, Blanco M, Pend'as AM, Costales A (1998) Quantum-mechanical study of thermodynamic and bonding properties of MgF2. J Phys Chem A 102:1595–1601
47. Petit AT, Dulong PL (1819) Recherches sur quelques points importants de la chaleur. Ann Chim Phys 10:395–413
48. Kamlesh PK, Agrawal R, Rani U, Verma AS (2022) Comprehensive ab-initio calculations of AlNiX (X = P, As and Sb) half-Heusler compounds: stabilities and applications as green energy resources. Mater Chem Phys 275:125233
49. Al-Qaisi S, Ali MA, Alrebdi TA, Vu TV, Morsi M, UlHaq B, Ahmed R, Mahmood Q, Tahir SA (2022) First-principles investigations of Ba_2NaIO_6 double perovskite semiconductor: material for low-cost energy technologies. Mater Chem Phys 275:125237
50. Pugh S XCII (1954) Relations between the elastic moduli and the plastic properties of polycrystalline pure metals. Lond Edinb Dublin Philos Mag J Sci 45:823–843
51. Pettifor D (1992) Theoretical predictions of structure and related properties of intermetallics. Mater Sci Technol 8:345–349
52. Vaitheeswaran G, Kanchana V, Svane A, Delin A (2007) Elastic properties of $MgCNi_3$ – a superconducting perovskite. J Phys Condens Matter 19:326214
53. Anderson OL, Demarest HH Jr (1971) Elastic constants of the central force model for cubic structures: polycrystalline aggregates and instabilities. J Geophys Res 76:1349–1369
54. Arikan N, Yildiz GD, Yildiz YG, İyigör A (2020) Electronic, elastic, vibrational and thermodynamic properties of HfIrX (X= as, Sb and Bi) compounds: insights from DFT-based computer simulation. J Electron Mater 49:1–11
55. Zhou D, Liu J, Xu S, Peng P (2012) Thermal stability and elastic properties of Mg_2X (X= Si, Ge, Sn, Pb) phases from first-principle calculations. Comput Mater Sci 51:409–414
56. Hoffmann A (1935) Examinations of compounds with Perovskite structure. Z Phys Chem 28:65–77
57. Knight K (1994) Structural phase transitions in $BaCeO_3$. Solid State Ionics 74:109–117
58. Knight KS (2001) Structural phase transitions, oxygen vacancy ordering and protonation in doped $BaCeO_3$: results from time-of-flight neutron powder diffraction investigations. Solid State Ionics 145:275–294
59 Genet F, Loridant S, Ritter C, Lucazeau G, Genet F, Loridant S, Ritter C, Lucazeau G (1999) Phase transitions in BaCeO3: neutron diffraction and Raman studies. J Phys Chem Solids 60:2009–2021
60. Stoffel RP, Dronskowski R (2013) First-principles investigations of the structural, vibrational and thermochemical properties of barium cerate–another test case for density-functional theory. Z Anorg Allg Chem 639:1227–1231
61. Zhang Q, Ding J, He M (2017) First principles study on structural, lattice dynamical and thermal properties of $BaCeO_3$. J Phys Chem Solids 108:76–81
62. Scaife DE, Weller PF, Fisher WG (1974) Crystal preparation and properties of cesium tin (II) trihalides. J Solid State Chem 9:308–314
63. Yamada K, Funabiki S, Horimoto H, Matsui T, Okuda T, Ichiba S (1991) Structural phase transitions of the polymorphs of $CsSnI_3$ by means of rietveld analysis of the X-ray diffraction. Chem Lett 20:801–804
64. Huang L-Y, Lambrecht WRL (2014) Lattice dynamics in perovskite halides $CsSnX_3$ with X= I Br, Cl. Phys Rev B 90:195201
65. Mori M, Masahiro, Saito H (1986) An X-ray study of successive phase transitions in CsSnBr 3. J Phys C: Solid State Phys 19:2391
66. Gesi K, Axe JD, Shirane G, Linz A (1972) Dispersion and damping of soft zone-boundary phonons in $KMnF_3$. Phys Rev B 5:1933–1941
67. Scott JF (1974) Soft-mode spectroscopy: experimental studies of structural phase transitions. Rev Mod Phys 46:83–128
68. Shirane G (1974) Neutron scattering studies of structural phase transitions at Brookhaven. Rev Modern Phys 46:437–449
69. Fujii Y, Hoshino S, Yamada Y, Shirane G (1974) Neutron-scattering study on phase transitions of $CsPbCl_3$. Phys Rev B 9:4549–4559
70. Woodward PM (1997) Octahedral tilting in perovskites. II. Structure stabilizing forces. Acta Crystallogr Sect B: Struct Sci 53:44–66